Constraining Black Hole Mass and Charge from Shadow and Inner Shadow Morphology

Julien Kearns

Advisor: Dr. Shane Davis

Department of Astronomy, University of Virginia

This thesis is submitted in partial completion of the requirement of the BS Astronomy-Physics Major.

May 9,2025

Draft version May 10, 2025
Typeset using LaTeX twocolumn style in AASTeX631

Constraining Black Hole Mass and Charge from Shadow and Inner Shadow Morphology

Julien A. Kearns,[1] Shane W. Davis,[1] Dominic O. Chang,[2,3] and Daniel C. M. Palumbo[3,4]

[1] Department of Astronomy, University of Virginia, Charlottesville, VA, 22904, USA
[2] Department of Physics, Harvard University, Cambridge, MA 02138, USA
[3] Black Hole Initiative At Harvard University, 20 Garden Street, Cambridge, MA 02138, USA
[4] Center for Astrophysics, Harvard & Smithsonian, 60 Garden Street, Cambridge, MA 02138, USA

ABSTRACT

We use ray-tracing techniques to investigate the morphology of the black hole shadow and inner shadow in the case of emission from thick and thin accretion disks in Schwarzchild and Reissner-Nordström spacetimes. Through these models we primarily study the effect of charge, observer inclination, and disk scaling ratio on the size and asymmetry of the inner shadow. We confirm that independent radii measurements of the shadow and inner shadow can constrain the mass and charge of a target Reissner-Nordström black hole with known viewing inclination. We also replicate these results to show similar constraints can be made on charge vs. inclination and charge vs. scale angle through the same process of independent measurements of the horizon radius and critical curve radius. We conclude that for sufficiently small scale angle, degeneracies between viewing inclination and scale angle can result in false constraints on the mass and charge.

1. INTRODUCTION

In 2017, The Event Horizon Telescope Collaboration (EHTC) made observations of the centers of the galaxy M87 and the Milky Way with a global array of radio telescopes utilizing Very Long Baseline Interferometry (VLBI) observing at 1.3 mm wavelengths (EHTC et al. 2019a,b; EHTC et al. 2022a). These observations were used to produce the first pictures of the near horizon region of the black holes M87* and Sgr A* (EHTC et al. (2019a,c); EHTC et al. (2022a,b)). The images depict ring-like features of ~ 40 μas in extent that have asymmetrical brightness distributions and are consistent with previous theoretical predictions of the appearances of black holes (Bardeen 1973; Luminet 1979; Falcke et al. 2000). These observations allowed the collaboration to establish constraints on the mass of M87* (see EHTC et al. 2019d, for their analysis) and the orientation of its spin axis with respect to Earth.

The ring-like features seen in black hole images are predicted to be composed of emission from multiple nested photon rings that converge in shape and size to a critical curve (Johnson et al. 2020; Gralla & Lupsasca 2020). The shape and morphology of photon rings are agnostic the underlying accretion physics, and are only sensitive to black hole mass, spin and charge (Walia 2024). These features suggest that photon ring measurements could be used to constrain black hole space time parameters. Individual photon rings are, however, likely unresolvable at the current nominal resolution of the instrument (reported to be ~ 25 μas in EHTC et al. 2019a).

Another image feature that has been predicted, but not yet observed, is the black hole inner shadow. The inner shadow is associated with the footprint of the jet on the black hole horizon seen at mm wavelengths. Chael et al. (2021) have suggested the inner shadow could serve as an additional probe of black hole space time properties. Measurements of the inner shadow would, however, require observations with high dynamic range that is challenging for the current EHT array.

Though not currently tractable, observations of the first photon ring and inner shadow are likely possible in the near future with VLBI observatories like the next generation EHT (ngEHT) and the Black Hole Explorer (BHEX) (Johnson et al. 2023; Johnson et al. 2024). Observations of these image features could therefore serve as constraints for measurements of black hole mass, spin and charge. Understanding how the size and morphology of these image features are linked to their underlying black hole parameters is therefore relevant.

This work focuses on constraints that can be derived from measurements of the critical curve and inner shadow around black holes. We will specifically focus on the case of a charged spherically symmetric black hole. Though we do not expect astrophysical black holes to carry much charge, some of the effects that electric charge has on the black hole images are similar to effects caused by spin. The additional symmetry afforded by our assumption allows for easier interpretation of some of these effects.

Corresponding author: Julien A. Kearns

In this paper we use a ray-tracing algorithm we develop in order to model null geodesics in spherically symmetric black hole spacetimes. In section 2, we describe the analytical basis behind key image features by studying the effective potential along the equatorial plane. In section 3, we introduce an analysis of the spacetime metric and the relevant derivations of a lens equation ($\frac{dr}{d\phi}$), radial potential ($R(r)$), and photon trajectories in the equatorial plane ($\phi(r)$). In section 4, we utilize an analytical solution to the spherically symmetric Reissner-Nordström spacetime metric tensor to generate numerical models using geodesics drawn from the observer. Emission is optically thin so photons are non-interacting. First we produce a model of the cross section of a black hole and accretion disk in 3-D space. Then we use the same algorithm to produce isoradial contours corresponding to the horizon radius and critical curve radius to simulate an image captured by an observer. In section 5, we generate a multitude of images across a range of charges, inclinations, scale angles and mass to distance ratios. Studying these models we draw constraints on the inner shadow and shadow morphology. In section 6, we use 2-D histograms to quantify the degeneracy of the inner shadow radius across charge, M/D, and scale angle. We normalize the histograms to show the probability density of models, which produces curves similar to the isoradial constraint curves in section 5.

2. IMAGES FEATURES OF BLACK HOLE ACCRETION SYSTEMS

We will discuss image features associated with the lensing of accretion disks around black holes. We will model our accretion as a axisymmetric disk whose emission extends down to the horizon. The disk will be taken to be thick and have boundaries that can be described by two identical, but oppositely oriented cones. The thickness of the cones will be parameterized by a 'scale angle'(or emission angle), c, which describes the angle made between a cone and the equatorial plane of the system. A positive scale angle means emission originates from a closer point than the equatorial plane, thus resulting in smaller inner shadow images.

2.1. *Photon Ring, Lensing, Shadow & Inner Shadow*

The photon ring consists of photons in bound orbits around a black hole, they can orbit the black hole many times before reaching the observer. A helpful feature of geodesics is that the path they trace scaterring away from a black hole is the same path they trace scattering towards a black hole. This means we can trace a geodesic backwards from the observer location to the critical curve, and observe as it asymptotically approaches a bound photon orbit Gralla et al. (2019).

The critical curve can be found with a method used in Luminet (1979). Trajectories on the equatorial plane ($\theta = \frac{\pi}{2}$) satisfy the differential equation:

$$\left[\frac{1}{r^2}\left(\frac{dr}{d\phi}\right)\right]^2 + \frac{1}{r^2}\left(1 - \frac{2M}{r}\right) = \frac{1}{b^2} \tag{1}$$

Where impact parameter $b = L/E$ and the second term on the left side can be interpreted as an effective potential $V(r)$ with a maximum at $r_c = 3M$.

$$b \leq [v(r)]^2 \tag{2}$$

$$V(r = 3m) = \frac{1}{27M^2} \tag{3}$$

so $b_c = 3\sqrt{3}M$ and $b > b_c$ trajectories are deflected while $b < b_c$ trajectories are captured.

The shadow is the area bounded by the critical curve, and the inner shadow is the area bounded by the event horizon which corresponds to $r = 2M$ in 3-D space for the Schwarzchild ($q = 0$) case.

3. FORMALISM

Here, we derive results that will be used to calculate photon geodesics in black hole space times with various astrophysical implications. We assume that the observer sits at radial infinity, and will only consider null geodesics in the black hole exterior that terminate at the observer.

3.1. *Null Geodesics in Spherically Symmetric Black Hole Space Times*

We will constrain the following discussion to a subclass of static, spherically symmetric, asymptotically flat metrics described by a line element with ansatz,

$$ds^2 = -f(r)dt^2 + \frac{dr^2}{f(r)} + r^2(d\theta^2 + \sin^2\theta d\phi^2), \tag{4}$$

where t is the time coordinate associated with an asymptotic observer far from the black hole, r is the areal radius of the space-time, θ and ϕ are the spherical inclination and azimuthal angles (see Appendix A for Schwarzschild metric). Null geodesics are required to have a zero line element, $ds^2 = 0$, and are associated with a conserved energy, E, and momentum, L, (see Appendix B for details on the derivation).

Conservation of angular momentum implies that photon geodesics are constrained to move in a plane that contains the black hole center as a point. If we assume that the photon's plane of motion is the equatorial plane of our coordinate choice, then Equation 4 can be brought to the form,

$$\frac{dr}{d\phi} = \frac{\sqrt{R(r)}}{b}, \tag{5}$$

where,

$$R(r) = \frac{E}{L}\sqrt{r^2\left(r^2 - f(r)\frac{L^2}{E^2}\right)}, \tag{6}$$

is the radial potential, and the conserved energy and angular momenta are given by

$$E = -f(r)\dot{t} \quad \text{and} \quad L = r^2\dot{\phi}. \tag{7}$$

The photon trajectories, in the equatorial plane can then be written as,

$$\phi(r) = \fint \frac{b}{\sqrt{R(r)}}\, dr, \tag{8}$$

where $\fint$ indicates a path dependent integral, and $b = \frac{L}{E}$ is the impact parameter of the photon.

Equation 8 can be re-parameterized into a non-path dependent expression, where we remind the reader that we are only considering photon trajectories that terminate at the asymptotic observer. First, we note that there are two types of relevant trajectories whose classification depend on the root structure of $R(r)$. Trajectories with radial potentials whose largest real root is behind the horizon—or with no real roots at all—will be called "plunging" trajectories, and those with radial potentials whose largest real root lies exterior to the horizon will be called "scattering" trajectories.

Plunging trajectories can be expressed as monotonic functions in r,

$$\phi_{\text{plunging}}(r) = \int \frac{b}{\sqrt{R(r)}} dr, \tag{9}$$

and thus do not have a path dependent integral. Scattering trajectories, on the other hand, have 2 values of $\phi_{\text{scattering}}$ associated with each $r > r_t$, where r_t is the largest real root of $R(r)$, and exactly one value of $\phi_{\text{scattering}}$ at $r = r_t$. These properties allow $\phi_{\text{scattering}}$ to be brought into a path-independent form by relating it to the pre-image of a parabola. We combine the properties of ϕ_{plunging} and $\phi_{\text{scattering}}$ to define $\phi(x)$ as,

$$\phi(x) = \int_{x_i}^{\infty} \frac{d\phi}{dx},\ dx \tag{10}$$

with,

$$\frac{d\phi}{dx} = \frac{-2b|x|}{(x^2+\tau)\sqrt{-\frac{(b^2)(-2+x^2+\tau)}{x^2+\tau} + (x^2+\tau)^2}}, \tag{11}$$

where x is related to r by,

$$r = x^2 + \tau \tag{12}$$

and,

$$\tau = \begin{cases} 0 & \text{plunging} \\ r_t & \text{scattering} \end{cases}. \tag{13}$$

3.2. *Reissner-Nordström Black Hole*

We will study some of the image features associated with accretion around an electrically charged, spherically symmetric black holes. The metric for this black hole is described by the Reissner-Nordström solution, (Reissner 1916; Weyl 1917; Nordström 1918) with line element is given by Equation 4 where

$$f(r) = 1 - \frac{2M}{r} + \frac{Q^2}{r^2}. \tag{14}$$

The Reissner-Nordström Black Hole has electric charge and no spin. In space, black holes are probably have little to no electric charge because any charge would quickly attract charged particles of the opposite sign and quickly neutralize it.

The Reissner-Nordström spacetime metric and radial potential are:

$$g_{\alpha\beta} = \begin{bmatrix} -(1-\frac{2M}{r}+\frac{Q^2}{r^2}) & 0 & 0 & 0 \\ 0 & \frac{1}{1-\frac{2M}{r}+\frac{Q^2}{r^2}} & 0 & 0 \\ 0 & 0 & r^2 & 0 \\ 0 & 0 & 0 & r^2\sin\theta^2 \end{bmatrix} \tag{15}$$

$$R(r) = r^2[r^2 - b^2(1 - \frac{2}{r} + \frac{Q^2}{r^2})] \tag{16}$$

3.3. *Winding Angle*

The winding angle describes the total angular displacement of a photon as it travels along a geodesic. In section 3, we analyze photon trajectories limited to the equatorial plane, for this case winding angle $\psi(r, b)$ simplifies to $\phi(r, b)$.

By generalizing (8) we get an expression for the winding angle, ψ:

$$\psi(r', b) = \int_{\infty}^{r} \frac{b}{\sqrt{R(r')}} dr' \tag{17}$$

We can simulate emission from an accretion disk by limiting the winding angle to one specified using coordinates in the bulk 3-D space: θ and ϕ, or θ and φ, the latter being the polar angle of a 2-D projection of the ray on an image screen at inclination θ_0. We used the following equations to write the winding angle ψ_{ss} and φ in terms of ϕ and θ:

$$\psi_{ss} = \arccos\left(\sin\theta_0 \sin\phi\right) \tag{18}$$

$$\varphi = \arctan\left(\tan\phi\cos\theta_0\right) \tag{19}$$

We used the root finding method of bisection through the Julia package *Roots.jl* to solve for r_s where $\psi(r, b) = \psi(\theta, \phi)$. The purpose of this function is to simulate an accretion disk from which the photons that reach the viewer originated. The radius at which the path of the ray is interrupted by the disk is the source radius, r_s.

3.4. *Scale Angle*

Next we modified the winding angle equation to include scale angle. This is the angle, c, above the plane of the accretion disk.

$$\theta_s = \frac{\pi}{2} - c \tag{20}$$

3.5. *Bridging Coordinate Systems*

In order to construct the models, an understanding of which coordinate systems are involved and at what stages is important. We want to produce an image in the 2-D image plane of an object that exists in 3-D bulk spacetime.

We begin on the image plane in Cartesian coordinates (x, y). On the coding level this looks like a meshgrid of X by Y pixels. We map the screen Cartesian coordinates to screen polar coordinates (φ, b), on the image plane the impact parameter, b, becomes our radius coordinate.

Next we choose our viewing inclination θ_s, and use θ_s and φ in equation (19) to find ϕ_s. Finally, we can use θ_s and ψ_s with equations (18) and (17) to solve for r_s, the source radius. After solving for r_s over all coordinates in the meshgrid we can produce contour plots.

4. MODELING

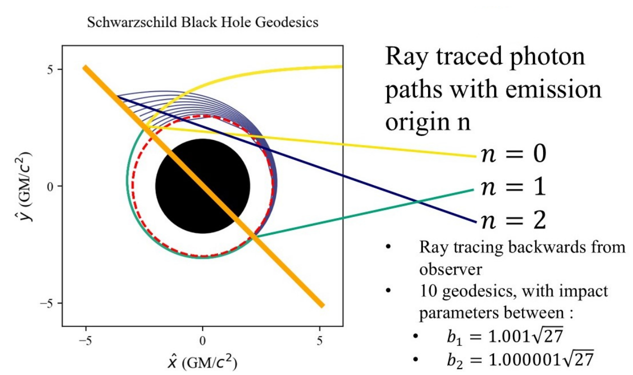

Figure 1. Cross section of 3-D black hole geometry. Critical curve radius in dashed red. Axes are in gravitational units because this models paths in bulk 3-D space. Geodesics are draw from a source observer at infinity (along the $n = 0$ geodesic). Viewing along the geodesic at infinity would reveal a lensed image of the black hole, distorting its true size.

Utilizing (11) and simulating equatorial emission we examine a cross section of the 3-D black hole geometry (Fig. 1). We examine emission from multiple points of origin and illustrate how $n > 0$ lines asymptotically converge at the critical curve radius r_c.

Using numerical solutions to photon geodesics around a black hole of mass M and charge $q = 0$, we generate isoradial contours of $n = 0$ scattered photon paths and $n = 1$ captured photon paths to model the black hole image features of the shadow (or the photon ring) and the inner shadow (Fig. 2). We vary across viewing inclination and scale angle to observe changes in inner shadow asymmetry and size.

The photon ring feature is caused by captured $n \geq 1$ orbits. In the spherically symmetric limit, critical curve radius is a function of M and q and therefore its appearance is always circular regardless of viewing inclination.

5. CONSTRAINTS

5.1. *Area & Asymmetry*

We observe how inner shadow asymmetry and area and changes across viewing inclination. We define a_h and b_h as the inner shadow principle axes (with $a_h = b_h$ when $i = 0°$ and $a_h \geq b_h$). We define asymmetry, α:

$$\alpha_h = \frac{a_h}{b_h} \tag{21}$$

We conclude inner shadow asymmetry is agnostic to changes in charge q and only dependent on changes in viewing inclination i (Fig. 3). The lack of degeneracy in asymmetry parameters means it is a reliable way to discern our viewing inclination through the image plane.

We find with increased viewing inclination, image plane measurements of the inner shadow area increase (Fig. 3). An increase in charge results in a decrease in observed inner shadow area. This bears similarity to the effects of spin in Kerr spacetime.

Emission angle, c, has no effect on inner shadow asymmetry.

The geometric impact of non-equatorial emission angles on inner shadow size is consistent with what we would expect from gravitational lensing effects.

5.2. *Charge Vs. Inclination*

Charge, q, and viewing inclination, i, both impact observed inner shadow area. This degeneracy means that there exists multiple combinations of q and i where $\overline{r_h}$ is the same. Utilizing ray-tracing models, we predict the value of $\overline{r_h}$ and $\overline{r_c}$ for a Reissner–Nordström black hole with parameters $q = .2$ and $i \approx 17°$.

To constrain q and i we measure $\overline{r_h}$ for all values in a 2D grid of q and i. This generates the heatmap (Fig. 4). Because the critical curve radius depends only on r, $\overline{r_c}$ is only dependant upon charge, q. Then we plot all combinations that return our target $\overline{r_h}$ and $\overline{r_c}$, this results in two isoradial charge vs. inclination curves that must intersect at the real physical values of these parameters, (Fig. 4). By observing the color blocking on the heatmap, we can observe how isoradial lines travel across the grid. Higher pixel resolution and higher variable resolution will increase the smoothness of the heatmap gradient and thus reveal isoradial trends clearer.

5.3. *Charge Vs. Mass*

To constrain M/D and q using high resolution observations, first measure mean inner shadow radius, $\bar{r}_h$,

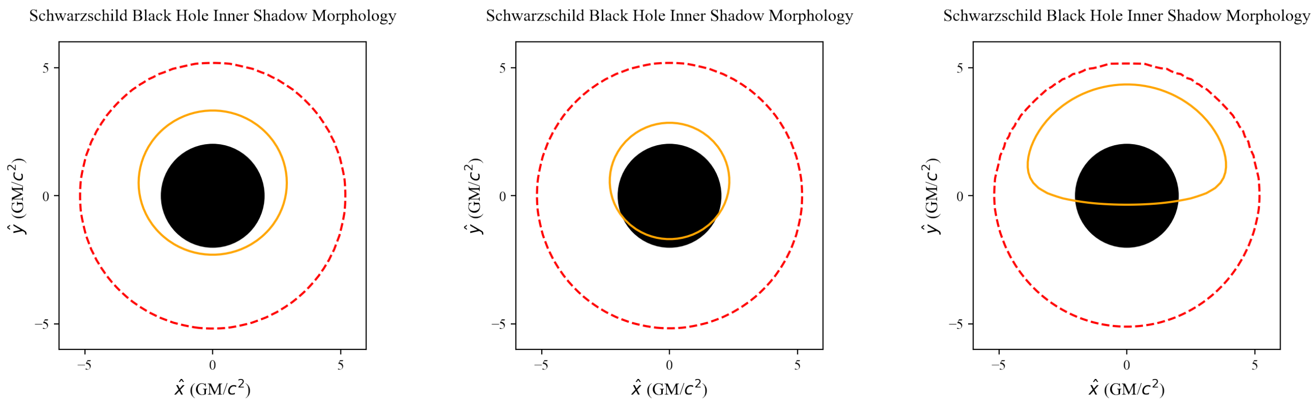

$\theta_s = 20°$, $c = 0°$ $\theta_s = 20°$, $c = 20°$ $\theta_s = 80°$, $c = 0°$

Figure 2. Critical curve (red, dashed lines) and inner shadow (orange lines) of accretion disks with varying scale angles around a Schwarzschild black hole as seen by observers at varying inclinations with respect to the symmetry axis of the accretion disk. The left and right panels show images seen by an observer viewing a thin disk accretion system at inclinations of 20° and 80° with respect to the symmetry axis of the disk. The center panel shows the images of the same system as the left panel, but for a thick accretion disk with a scale angle of 20°. The image of the black hole horizon, a radius of $r_h = 2GM/c^2$, in the absence of gravitational lensing is shown for scale (solid black disk)

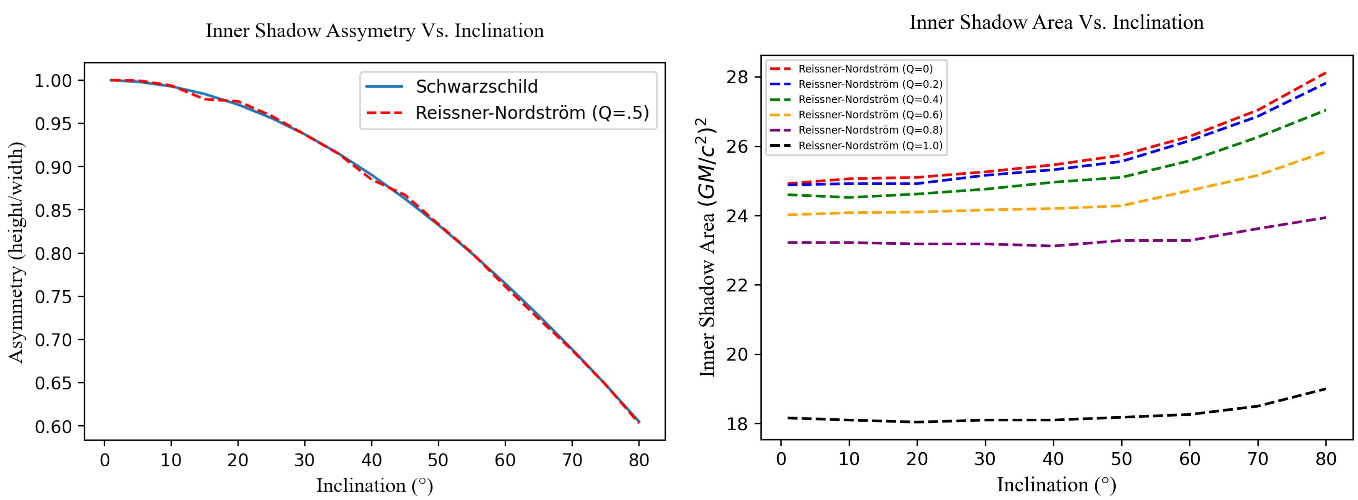

Figure 3. (Left) α_h vs. i for a neutral ($q = 0$) Schwarzschild black hole and a Reissner–Nordström black hole with charge $q = .5$. The decreasing curve reveals a unique asymmetric value for each inclination. Due to the asymmetry causing an uneven radius along the lensed horizon, we rely on the average horizon radius $\overline{r_h}$ for later analysis. (Right) Inner shadow area in gravitational units vs. inclination across 6 different Reissner–Nordström black hole charges. These curves reveal inner shadow area increases with viewing inclination, the increase is steeper at higher inclinations. They also reveal that area decreases with charge. This relation is not linear as the difference in size between $q = 1$ and $q = .8$ is much larger than $q = 0$ and $q = .2$.

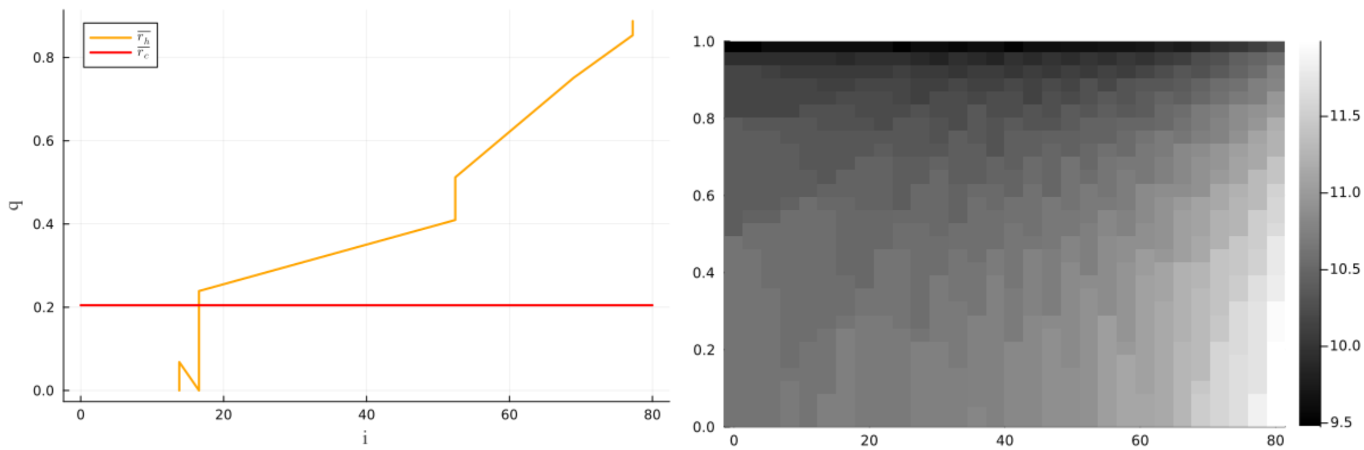

Figure 4. (Left) Constraints on black hole viewing inclination, i, and charge, q, by independent measurements of the average radii of the lensed horizon, $\overline{r_h}$, and critical curve, $\overline{r_c}$. The input charge was $q = .2$ and the inclination $\theta \approx 20°$. The $\overline{r_c}$ curve is linear because critical curve radius is independent of viewing inclination. Whereas the $\overline{r_h}$ is jagged, which reveals the necessity for a higher grid resolution. (Right) Heatmap of all potential $\overline{r_h}$ values across grid of inclinations and charges. There are two factors that can increase heatmap resolution: pixel resolution (the amount of pixels per variable grid) and variable resolution (the amount of q or i values we model over).

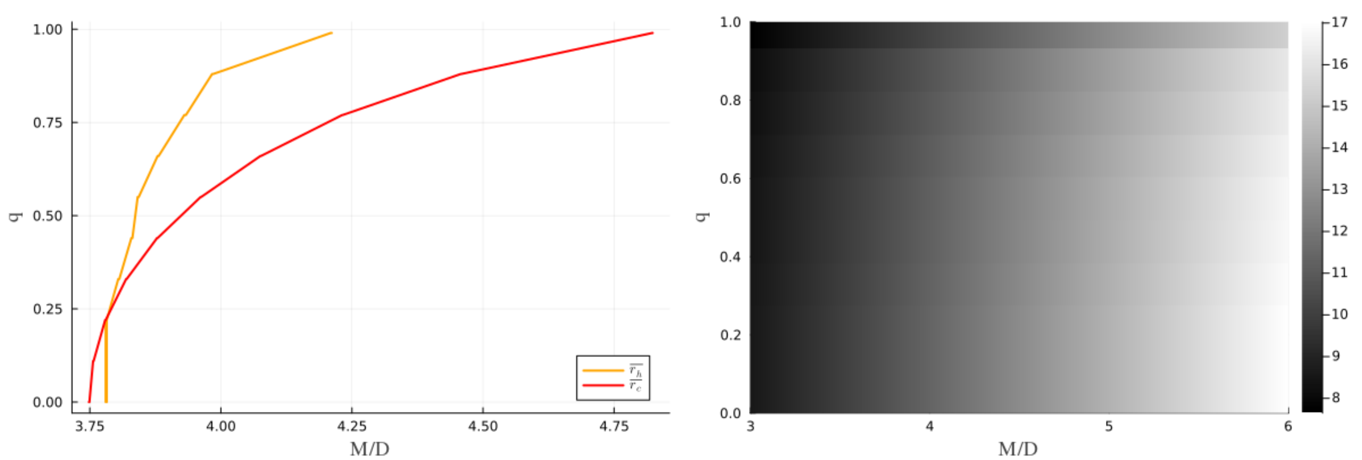

Figure 5. (Left) Constraints on black hole mass to distance ratio, M/D, and charge, q, by independent measurements of the average radii of the lensed horizon, $\overline{r_h}$, and critical curve, $\overline{r_c}$. The input charge was $q \approx .2$ with $M/D = 3.78$. The curved nature of both plots reveal how isoradial contours travel along the parameter space of q and M/D. This also means $\overline{r_c}$ is impacted by both variables. (Right) Heatmap of all potential $\overline{r_h}$ values across grid of mass and charge. We confirm the shape of our constraint plot by analyzing that larger horizon radius values lie on the bottom right of the plot, and smaller value lies on the top left. Our constraint curves lie in between these corners, tracing isoradial parameter pairs.

and mean critical curve radius, $\bar{r_c}$, for all values of a 2D grid of M/D and q values with a given viewing inclination $i = 20°$. Plot all combinations that return a given $\overline{r_h}$ and $\overline{r_c}$, this results in two isoradial mass vs. charge curves that must intersect at the real physical values of these parameters (Fig. 5).

Analogous Kerr models by Chael et al. (2021) assume equatorial emission, we show how changes in emission angle can skew isoradial horizon curves and translate the $\bar{r_h}$ curve in the q vs. M/D plots (Fig. 6). We conclude that for sufficiently small emission angle, degeneracies between viewing inclination and emission angle can result in false constraints on M and q when fitting data to an equatorial model.

5.4. *Charge Vs. Emission Angle*

Using similar techniques, we construct a constraint plot across emission angle, c, and black hole charge, q, that intends to simulate results from independent observations of $\overline{r_h}$ and $\overline{r_c}$, (Fig. 7). Experimentally, the EHT would be most sensitive to positive scale heights which result in smaller and brighter inner shadows. Though the detector may pick up emission from a negative scale height, when researchers extract horizon radius from image plane measurements they might not identify the negative scale height emission as the inner shadow because it would not be bounding the brightness depression associated with the horizon. To maintain consistency with prior constraint plots and to continue to fit according to equatorial emission models, I include negative scale heights and generate a characteristic isoradial curve. The heatmap reveals isoradial curves follow the same shape across the grid.

6. QUANTIFYING INNER SHADOW RADIUS DEGENERACY

We have introduced four distinct parameters that impact observed inner shadow area, which thus impacts calculated inner horizon radius. Black hole charge, q, and mass to distance ratio, M/D, impact both the inner horizon radius as well as the critical curve radius. Utilizing a modified version of (2.1) specific to the Reissner-Nordström metric, we can the effectuve potential $V(q, r)$ to produce an expression for $r_c(q)$:

$$r_c(q) = \frac{\sqrt{27 - 36q^2 + 8q^4 + (9 - 8q^2)^{\frac{3}{2}}}}{\sqrt{2}\sqrt{1 - q^2}} \tag{22}$$

Viewing inclination. i, and emission angle, c, both only impact inner shadow radius. Luckily, inner shadow asymmetry is dependent only on viewing inclination, as seen in Figure 3, so theoretically with higher resolution we will be able to discern our viewing inclination solely through observations of the asymmetry. Emission angle impacts inner shadow radius linearly, thus $\overline{r_h}(c)$ can be easily recomputed according to a scale factor inversely proportional to c.

Given high resolution independent observations of a black hole shadow and inner shadow, after deducing inclination angle we are left with some uncertainty in M/D, q, and c. We plot a 2-D histogram of all potential $\overline{r_h}$ and $\overline{r_c}$ values, then zoom into a region centered on $\overline{r_{h,observed}}$ and $\overline{r_{c,observed}}$ with a 10% range of error (Fig. 8). Through this 2-D histogram we observe a bright linear ridge, and there appears to be more samples on one side than the other. Did this statistical skew arise due to our choice of parameter ranges?

In order to study the probability distribution of potential inner shadow models, we will trim the master histogram and only keep $\overline{r_h}$ values that are within 10% of $\overline{r_{h,observed}}$, which we calculate using the parameters $q = .2$, $c = 0°$, $i = 0°$, $M/D = 3.78\mu as$. We produce three normalized 2-D histograms (Fig. 9) to reveal probability regions of high density for all 3 degenerate parameters.

7. CONCLUSION

Explorations of numerical Reissner-Nordström black hole models reveal constraints on the morphology of two key image features: the black hole shadow and inner shadow. Constraints on these image features are driven by their relativistic phenomenology. The inner shadow is bounded by the black hole horizon radius. The asymmetry of the horizon on the image plane is dependent on the viewing inclination of the observer. The area, and thus the radius, of the inner shadow decreases with increasing charge for any constant mass to distance ratio. The case is the same for the shadow, whose radius is determined by the critical curve radius which is derived from the effective potential $V(r, q)$. Charge, q, and mass to distance ratio, M/D affect both r_h and r_c. Emission angle, c, and viewing inclination, i, only affect r_h. We confirm that independent radii measurements of the shadow and inner shadow can constrain the mass and charge of a target Reissner-Nordström black hole with known viewing inclination. These results are analogous to Chael et al. (2021), which proves the same constraints can be made on a Kerr black hole with mass and spin. I replicate these results to show similar constraints can be made on q vs. i and q vs. c through the same process of independent measurements of r_h and r_c. By attempting to fit $r_{h,observed}$ from emission with some $c \neq 0°$ to a model assuming equatorial emission ($c = 0°$), we conclude that for sufficiently small emission angle, degeneracies between viewing inclination and emission angle can result in false constraints on the mass and charge.

APPENDIX

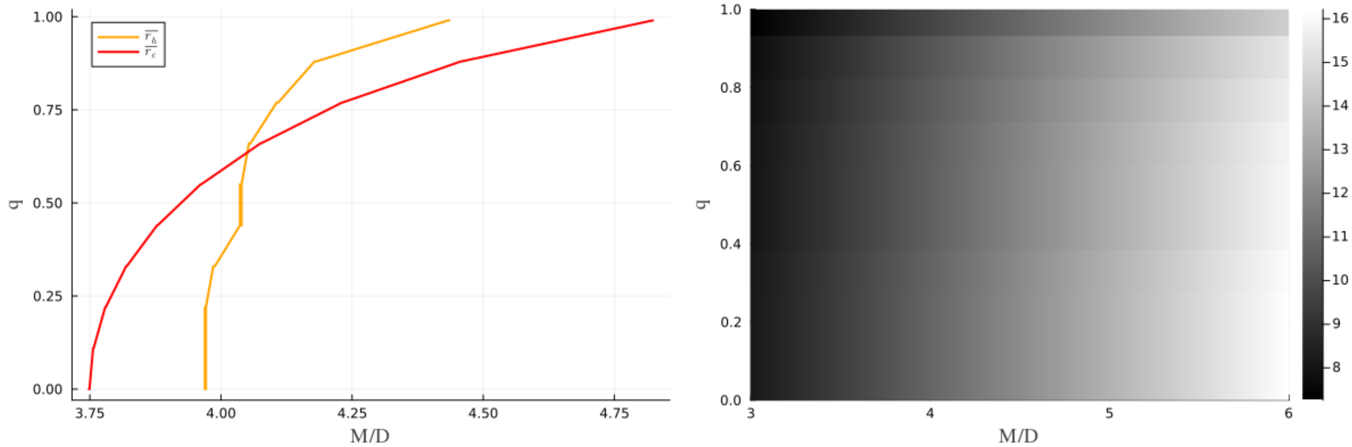

Figure 6. (Left) False constraints on black hole mass to distance ratio, M/D, and charge, q, by independent measurements of the average radii of the lensed horizon, $\overline{r_h}$, and critical curve, $\overline{r_c}$ when emission angle $c = 5°$. The input charge was $q \approx .2$ with $M/D = 3.78$ and assuming $c = 0°$. The $\overline{r_c}$ curve remains in the same place as in 5.3 which reveals the critical curve radius is not impacted by emission with some scale angle. The $\overline{r_h}$ curve is shifted to the right towards higher M/D when fitting with the same values as 5.3 which reveals that $c > 0°$ causes a decrease in horizon radius.(Right) Heatmap of all potential $\overline{r_h}$ values across grid of mass and charge with $c = 5°$.

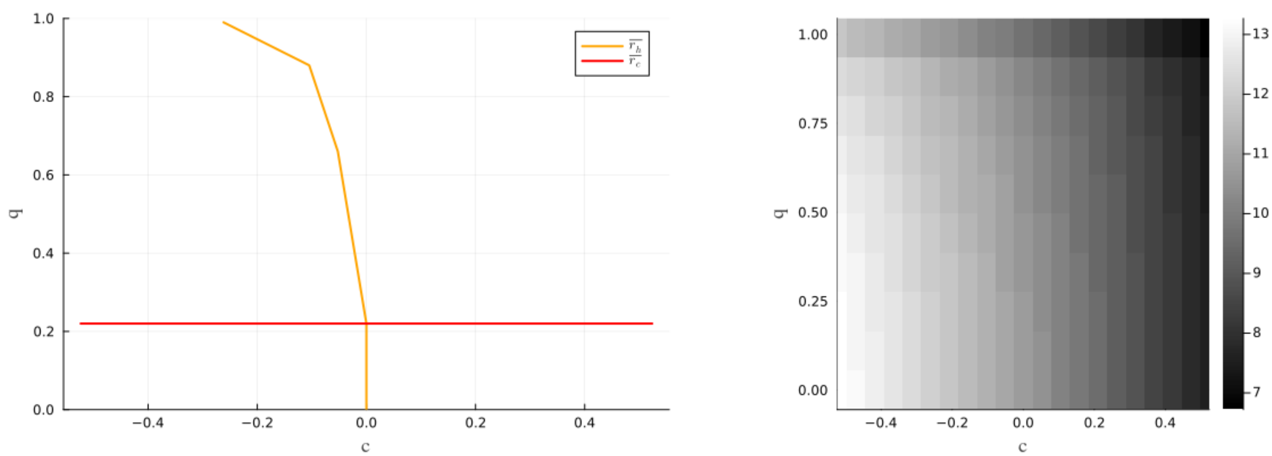

Figure 7. (Left) Constraints on black hole emission angle, c, and charge, q, by independent measurements of the average radii of the lensed horizon, $\overline{r_h}$, and critical curve, $\overline{r_c}$. The input charge was $q \approx .2$ with $c = 0°$. The $\overline{r_c}$ curve is linear because critical curve radius is independent of scale angle.(Right) Heatmap of all potential $\overline{r_h}$ values across grid of emission angle and charge. This heatmap reveals larger values lie in the bottom left corner where charge is small and scale angle is negative.

A. SCHWARZSCHILD BLACK HOLE METRIC

The spacetime metric and radial potential unique to a Schwarzschild model is:

$$g_{\alpha\beta} = \begin{bmatrix} -1 - \frac{2M}{r} & 0 & 0 & 0 \\ 0 & \frac{1}{1-\frac{2M}{r}} & 0 & 0 \\ 0 & 0 & r^2 & 0 \\ 0 & 0 & 0 & r^2 \sin\theta^2 \end{bmatrix} \tag{A1}$$

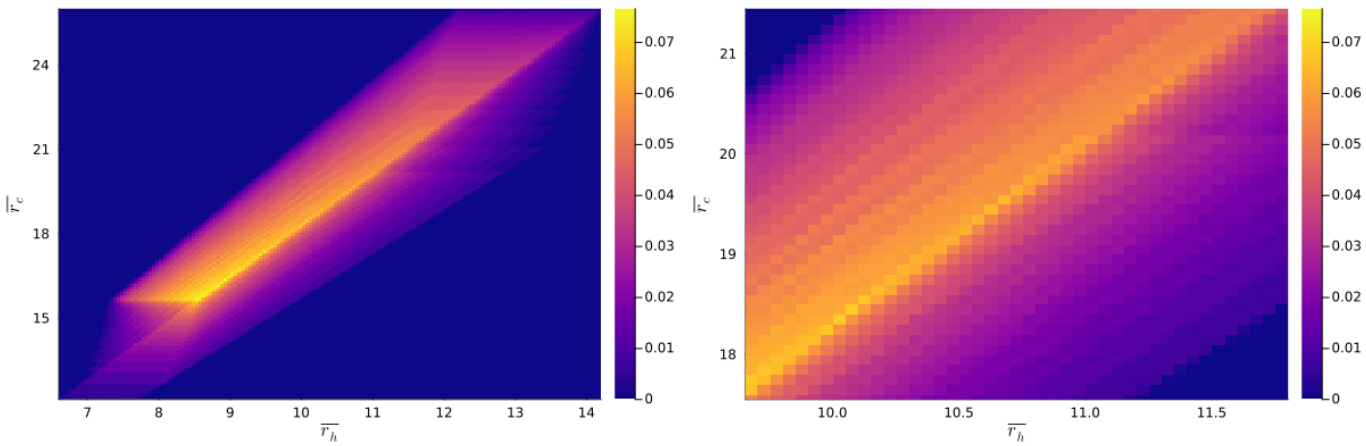

Figure 8. (Left) 2-D normalized histogram constructed with all possible values of $\overline{r_h}$ and $\overline{r_c}$ given $M/D \in [3,5]$, $q \in [0,1]$, $c \in [0, 15°]$, and $i = 0°$ (Right) Same histogram zoomed in around calculated $\overline{r_{h,observed}}$ and $\overline{r_{c,observed}}$ using the parameters $q = .2$, $c = 0°$, $i = 0°$, $M/D = 3.78\mu as$, with a 10% range of error.

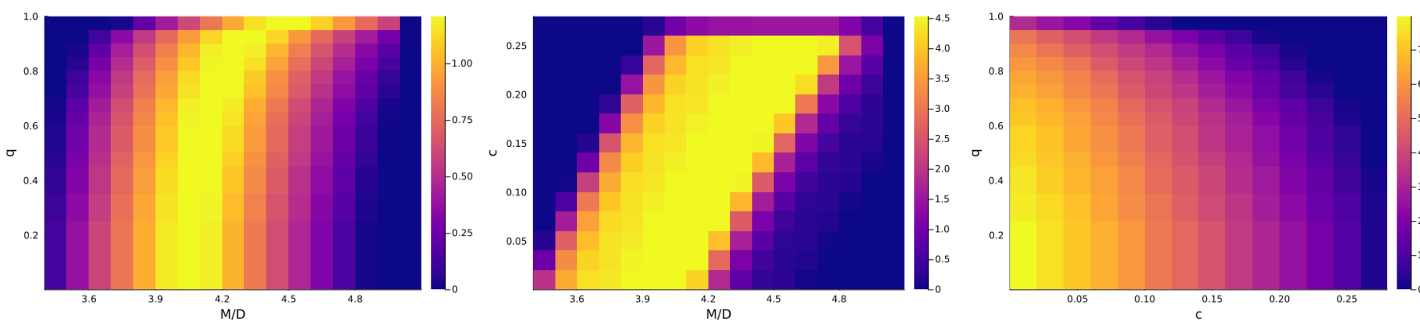

$q \in [0,1]$ vs. $M/D \in [3,5]$ $\quad$ $c \in [0, \pi/12]$ vs. $M/D \in [3,5]$ $\quad$ $q \in [0,1]$ vs. $c \in [0, \pi/12]$

Figure 9. Normalized 2-D histograms (using data from 6) marginalized over key degenerate parameters q, c, and M/D to show probability density of models that fit within 10% of $\overline{r_{h,observed}}$. On the left plot we notice a curve similar to 5.3 which confirms the shape of an isoradial contour in the 2-D parameter space q vs. M/D. The center plot does not have an analogous constraint plot but due to the nature of the histogram it should reveal the shape of the isoradial horizon contour on a constraint plot of c vs. M/D, we would expect the critical curve contour to be a horizontal line similar to in 5.4. The right plot resembles the heat map in 5.4 but it provides a zoomed in view around a smaller interval. We can see when c becomes too large and thus does not yield any models within the 10% confidence range.

$$g^{\alpha\beta} = \begin{bmatrix} -\frac{1}{1-\frac{2M}{r}} & 0 & 0 & 0 \\ 0 & 1-\frac{2M}{r} & 0 & 0 \\ 0 & 0 & \frac{1}{r^2} & 0 \\ 0 & 0 & 0 & \frac{1}{r^2\sin\theta} \end{bmatrix} \tag{A2}$$

$$R(r) = r^4 - b^2r^2 + 2b^2r \tag{A3}$$

The metric can be written in terms of ds:

$$ds^2 = -(1-\frac{2M}{r})dt^2 + \frac{1}{1-\frac{2M}{r}}dr^2 + r^2d\theta^2 + r^2sin^2d\phi^2 \tag{A4}$$

B. DERIVING CONSERVATION LAWS

To derive the the law of conservation of energy and the law of conservation of angular momentum we must write dS using the metric tensor:

$$dS = \sqrt{g_{\alpha\beta} dq^{\alpha} dq^{\beta}} = \sqrt{g_{\alpha\beta} \frac{dq^{\alpha}}{d\tau} \frac{dq^{\beta}}{d\tau}} d\tau \tag{B5}$$

Then we take the variation and set it equal to 0:

$$\delta S = \int \delta L \, d\tau = \int \frac{\delta L'}{L} \, d\tau = 0 \tag{B6}$$

$$L' = (1/2) g_{\alpha\beta} \dot{q}^{\alpha} \dot{q}^{\beta} = 0 \tag{B7}$$

Convert to Hamiltonian coordinates:

$$L' = \frac{1}{2} g_{\alpha\beta} \dot{q}^{\alpha} \dot{q}^{\beta} = H = \frac{1}{2} g^{\alpha\beta} p_{\alpha} p_{\beta} = 0 \tag{B8}$$

By writing the action in terms of the Hamiltonian, we can define two important relationships (B11):

$$S = \int L d\tau = \int (p\dot{q} - H) d\tau \tag{B9}$$

$$\delta S = 0 \rightarrow (\dot{q} - \frac{\partial H}{\partial p})\delta p + (\delta \dot{q} p - \frac{\partial H}{\partial q} \delta q = 0 \tag{B10}$$

$$\frac{\partial H}{\partial p} = \dot{q}, \frac{\partial H}{\partial q} = -\dot{p} \tag{B11}$$

Next we evaluate $\frac{\partial H}{\partial q}$ with $q = \phi$ and $q = t$, keeping in mind what components define the metric tensor:

$$g^{\alpha}\beta(r, \theta) \rightarrow \frac{\partial H}{\partial \phi} = -\dot{p}_{\phi} = 0, \frac{\partial H}{\partial t} = -\dot{p}_{t} = 0 \tag{B12}$$

These respective results prove angular momentum is conserved, and energy is conserved over time.

REFERENCES

Bardeen, J. M. 1973, in Black Holes (Les Astres Occlus), 215–239

Chael, A., Johnson, M. D., & Lupsasca, A. 2021, The Astrophysical Journal, 918, 6, doi: 10.3847/1538-4357/ac09ee

EHTC, Akiyama, K., Alberdi, A., et al. 2019a, The Astrophysical Journal Letters, 875, L1, doi: 10.3847/2041-8213/ab0ec7

—. 2019b, The Astrophysical Journal Letters, 875, L2, doi: 10.3847/2041-8213/ab0c96

—. 2019c, The Astrophysical Journal Letters, 875, L4, doi: 10.3847/2041-8213/ab0e85

—. 2019d, The Astrophysical Journal Letters, 875, L6, doi: 10.3847/2041-8213/ab1141

EHTC, Akiyama, K., Alberdi, A., et al. 2022a, ApJL, 930, L12, doi: 10.3847/2041-8213/ac6674

—. 2022b, ApJL, 930, L14, doi: 10.3847/2041-8213/ac6429

Falcke, H., Melia, F., & Agol, E. 2000, ApJL, 528, L13, doi: 10.1086/312423

Gralla, S. E., Holz, D. E., & Wald, R. M. 2019, Physical Review D, 100, doi: 10.1103/physrevd.100.024018

Gralla, S. E., & Lupsasca, A. 2020, Phys. Rev. D, 101, 044031, doi: 10.1103/PhysRevD.101.044031

Johnson, M. D., Doeleman, S. S., Gómez, J. L., & Broderick, A. E. 2023, Galaxies, 11, doi: 10.3390/galaxies11050092

Johnson, M. D., Lupsasca, A., Strominger, A., et al. 2020, Science Advances, 6, eaaz1310, doi: 10.1126/sciadv.aaz1310

Johnson, M. D., Akiyama, K., Baturin, R., et al. 2024, in Society of Photo-Optical Instrumentation Engineers (SPIE) Conference Series, Vol. 13092, Space Telescopes and Instrumentation 2024: Optical, Infrared, and Millimeter Wave, ed. L. E. Coyle, S. Matsuura, & M. D. Perrin, 130922D, doi: 10.1117/12.3019835

Luminet, J. P. 1979, A&A, 75, 228

Nordström, G. 1918, Koninklijke Nederlandse Akademie van Wetenschappen Proceedings Series B Physical Sciences, 20, 1238

Reissner, H. 1916, Annalen der Physik, 355, 106, doi: https://doi.org/10.1002/andp.19163550905

Walia, R. K. 2024, Physical Review D, 110, doi: 10.1103/physrevd.110.064058

Weyl, H. 1917, Annalen der Physik, 359, 117, doi: https://doi.org/10.1002/andp.19173591804